Results in Physics 29 (2021) 104767

Contents lists available at ScienceDirect

Results in Physics

journal homepage: www.elsevier.com/locate/rinp

High sensitivity temperature sensor based on a helically twisted photonic crystal fiber

Shi Qiu [a], Jinhui Yuan [a,b,*], Sainan Duan [a], Xian Zhou [b], Chao Mei [b], Yuwei Qu [a], Binbin Yan [a], Qiang Wu [c,d,*], Kuiru Wang [a], Xinzhu Sang [a], Keping Long [b], Chongxiu Yu [a]

[a] State Key Laboratory of Information Photonics and Optical Communications, Beijing University of Posts and Telecommunications, Beijing 100876, China
[b] Research Center for Convergence Networks and Ubiquitous Services, University of Science & Technology Beijing, Beijing 100083, China
[c] Department of Physics and Electrical Engineering, Northumbria University, Newcastle upon Tyne NE1 8ST, United Kingdom
[d] Key Laboratory of Optoelectronic Information Science and Technology of Jiangxi Province, Nanchang Hangkong University, Nanchang 330063, China

ARTICLE INFO

Keywords:
Helically twisted photonic crystal fiber
Finite element method,
Surface plasmon resonance
Temperature sensor

ABSTRACT

Helically twisted photonic crystal fibers (HT-PCFs) provide additional opportunities for controlling the light propagation characteristics and improving the sensing performances. In this paper, a toluene and gold wire-filled HT-PCF was proposed and designed for high sensitivity temperature sensing. The influences of the structure parameters on the confinement loss, sensitivity, and resolution of the proposed HT-PCF were investigated. For the optimized HT-PCF, the average sensitivity is as high as 14.35 and 17.29 nm/℃ in the temperature range of −20 to 20 ℃ and 20 to 70 ℃, respectively. Moreover, the proposed HT-PCF-based temperature sensor is insensitive to the hydrostatic pressure. Finally, the detailed fabrication process of the toluene and gold wire-filled HT-PCF temperature sensor is proposed. It is believed that the proposed HT-PCF temperature sensor has potential applications in the fields of the environmental monitoring, medical diagnostics, etc.

Introduction

Photonic crystal fibers (PCFs) have attracted significant attentions owing to their unique optical properties and high flexibility in design [1,2]. Helically twisted PCF (HT-PCF) is a new kind of PCF, in which the conventional linearly polarized (LP) mode can be split in two circularly polarized modes: right-circularly polarized (RCP) mode and left-circularly polarized (LCP) mode [3]. The helically twisted structure breaks the cylindrical symmetry and creates different propagation conditions for the RCP and LCP modes. Thus, the striking transmission behaviors of light in the HT-PCF could find important applications in sensing parameters, including temperature [4], torsion and strain [5,6], current and magnetic field [7,8], etc. Among them, the temperature is the most common parameter in almost everywhere, such as the environmental monitoring, etc.

In recent years, some effective methods have been reported to improve the sensitivity of the PCF-based temperature sensor, including infill of the temperature sensitive liquid (TSL), excitation of surface plasmon resonance (SPR), combination of the TSL and SPR effect [9,10], etc. In 2015, Liu *et al.* studied a TSL filled SPR sensor, whose average sensitivity was −2.15 nm/°C in the temperature range from 20 to 80 °C [11]. In 2016, Liu *et al.* proposed a liquid filled twin-core fiber sensor with an average sensitivity of 1.23 nm/°C, in a wide temperature range of 25 to 50 °C [12]. In 2017, Ma *et al.* demonstrated a toluene filled PCF sensor, where the average sensitivity of −6.25 nm/℃ for the temperature range of 0 to 90 °C has been achieved [14]. In 2018, Yang *et al.* demonstrated that by filling TSL into a hollow-core fiber, the average sensitivity could be as high as 6.51 nm/°C in temperature range from 20 to 100 °C [15]. In 2019, Liu *et al.* developed a gold-coated D-shaped PCF sensor, where the average sensitivity could be up to 10.61 nm/°C in the temperature range from 0 to 60 °C [17]. In 2020, Zhao *et al.* reported that by filling glycerin in a polarization-maintaining PCF sensor, the highest sensitivity could reach 1.5005 nm/°C in a wide temperature range of −25 to 85 °C [18]. The above sensors are based on modifications of the two-dimensional structures of the PCFs, which have limitations for further improving the temperature sensitivity, and thus three-

* Corresponding authors at: State Key Laboratory of Information Photonics and Optical Communications, Beijing University of Posts and Telecommunications, Beijing 100876, China; Research Center for Convergence Networks and Ubiquitous Services, University of Science & Technology Beijing, Beijing 100083, China (J. Yuan). Department of Physics and Electrical Engineering, Northumbria University, Newcastle upon Tyne NE1 8ST, United Kingdom; Key Laboratory of Optoelectronic Information Science and Technology of Jiangxi Province, Nanchang Hangkong University, Nanchang 330063, China (Q. Wu).
E-mail addresses: yuanjinhui81@bupt.edu.cn (J. Yuan), qiang.wu@northumbria.ac.uk (Q. Wu).

https://doi.org/10.1016/j.rinp.2021.104767
Received 5 July 2021; Received in revised form 25 August 2021; Accepted 26 August 2021
Available online 31 August 2021

dimensional design of PCF structure has been proposed. For example, in [19,20], a novel three-dimensional helical symmetry HT-PCFs has been the experimentally demonstrated, that has relatively high temperature sensitivity compared with the conventional two-dimensional PCFs.

In this paper, a toluene and gold wire-filled HT-PCF was proposed and theoretically investigated as a temperature sensor. In our design, the toluene is filled into the central air hole and a gold wire is filled in a cladding air hole. The simulation results show that the toluene and gold wire-filled HT-PCF has great advantage on improving the temperature sensitivity. The average sensitivity could be as high as 14.35 and 17.29 nm/℃ in the temperature ranges of −20 to 20 ℃ and 20 to 70 ℃, respectively. Moreover, the sensitivity to hydrostatic pressure was also investigated, and the average sensitivity is only −214.3 pm/MPa in the hydrostatic pressure range of 0 to 50 MPa, which means that the hydrostatic pressure has limited influence on the temperature sensor. Finally, the fabrication processes of the toluene and gold wire-filled HT-PCF temperature sensor was proposed and discussed.

Design of the toluene and gold Wire-Filled HT-PCF and theory

Fig. 1(a) shows the three-dimensional diagrammatic sketch of the proposed toluene and gold wire-filled HT-PCF. Fig. 1(b) and 1(c) show the LCP and RCP modes, respectively. In the simulation, the rotate direction of the fiber is assumed to be clockwise as illustrated by the red arrow. Fig. 2(a) shows the diagrammatic sketch of the cross-section of the proposed toluene and gold wire-filled HT-PCF, where the material is the silica with the refractive index (RI) of n_{silica} and the hole to hole distance is set as Λ. The diameter of the cladding air holes is set as d_a. In our design, the fiber core is formed by a toluene-filled hole, whose RI and diameter are set as n_t and d_t, respectively. The air hole in the second layer below the core is a gold wire filled hole, whose permittivity and diameter are set as ε_g and d_g, respectively. The twist direction is clockwise along the z direction, and the corresponding twist rate is set as α. In the simulation, the FEM is used and the grid size of the whole model is set as $\lambda/4$. Fig. 2(b) and 2(c) are the Poynting vector distributions of the RCP and LCP of the core mode. Toluene is a kind of common temperature sensitive liquid, and its thermos-optic coefficient (σ) can be up to 3.94×10^{-4} /°C, which means that the temperature change will significantly change the RI of the toluene. In the previous studies, the good temperature sensing performance of the toluene has been proved [15,21].

The relationship between the helical coordinates (ξ_1, ξ_2, ξ_3) and Cartesian coordinates (x, y, z) is described as [22,23]

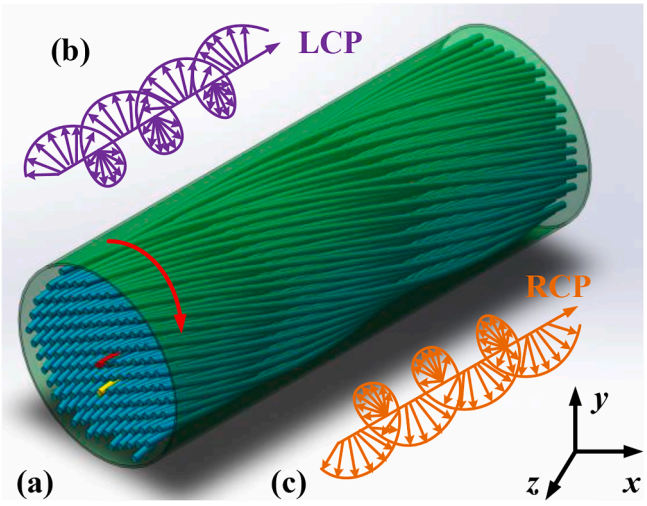

Fig. 1. (a) The three-dimensional diagrammatic sketch of the proposed toluene and gold wire-filled HT-PCF, and (b) and (c) show the LCP and RCP modes, respectively.

$$\begin{cases} x = \xi_1 cos(\alpha\xi_3) + \xi_2 sin(\alpha\xi_3) \\ y = -\xi_1 sin(\alpha\xi_3) + \xi_2 cos(\alpha\xi_3) \\ z = \xi_3 \end{cases} \tag{1}$$

The general coordinate system can be characterized by the Jacobian (J_t) of the transformation in Eq. (1)

$$J_t(\xi_1,\xi_2,\xi_3) = \frac{\partial(x,y,z)}{\partial(\xi_1,\xi_2,\xi_3)} = \begin{pmatrix} cos(\alpha\xi_3) & sin(\alpha\xi_3) & \alpha\xi_2 cos(\alpha\xi_3) - \alpha\xi_1 sin(\alpha\xi_3) \\ -sin(\alpha\xi_3) & cos(\alpha\xi_3) & -\alpha\xi_1 cos(\alpha\xi_3) - \alpha\xi_2 sin(\alpha\xi_3) \\ 0 & 0 & 1 \end{pmatrix} \tag{2}$$

For a twisted structure, the permittivity ε, the permeability μ and the boundary conditions only depend on the ξ_1 and ξ_2. Both the two coordinates can satisfy the wave equation, due to the equivalence under the coordinate transformation of Maxwell's equations

$$\nabla \times \left(\mu_t^{-1} \nabla \times \boldsymbol{E}\right) - k_0^2 \varepsilon_t \boldsymbol{E} = 0 \tag{3}$$

where E stands for the electric field vector, k_0 is the free-space wavenumber, and ε_t and μ_t represent the relative permittivity and permeability tensors in the helical coordinates, respectively. In the simulation, the original permittivity and permeability (ε, μ) should be replaced by the helically inhomogeneous anisotropic tensors (ε_t, μ_t). The corresponding transformation relations are described as follows [24]

$$\varepsilon_t = \varepsilon T^{-1}, \mu_t = \mu T^{-1}, \tag{4}$$

where the transformation matrix T and its inverse matrix T^{-1} can be described as[25,26]

$$T_t(\xi_1,\xi_2) = \frac{J_t^T J_t}{det(J_t)} = \begin{pmatrix} 1 & 0 & \alpha\xi_2 \\ 0 & 1 & -\alpha\xi_1 \\ \alpha\xi_2 & -\alpha\xi_1 & 1+\alpha^2(\xi_1^2+\xi_2^2) \end{pmatrix} \tag{5}$$

$$T_t^{-1}(\xi_1,\xi_2) = \begin{pmatrix} 1+\alpha^2\xi_2^2 & -\alpha^2\xi_1\xi_2 & -\alpha\xi_2 \\ -\alpha^2\xi_1\xi_2 & 1+\alpha^2\xi_1^2 & \alpha\xi_1 \\ -\alpha\xi_2 & \alpha\xi_1 & 1 \end{pmatrix} \tag{6}$$

Eq (6) is a symmetric matrix, so it is equivalent for the left and right rotation conditions.

To simulate on the two-dimensional structure of the PCF, the Cartesian coordinate system needs to be transformed into a helical coordinate system, while ξ_1 and ξ_2 do not exist in the Cartesian coordinate system in Eq. (6). Thus, according to Eq. (1), ξ_1, ξ_2, and ξ_3 are defined as [27]

$$\begin{cases} \xi_1 = \dfrac{xcos(\alpha z) - ysin(\alpha z)}{cos(\alpha z)} \\ \xi_2 = \dfrac{ycos(\alpha z) - xsin(\alpha z)}{cos(2\alpha z)} \\ \xi_3 = z \end{cases} \tag{7}$$

For the temperature sensing, n_{silica} of the temperature-dependent Sellmeier equation can be expressed as [28,29]

$$n_{\text{silica}}^2 = \left(1.31522 + 6.90754\times10^{-6}T\right) + \frac{\left(0.788404 + 23.5835\times10^{-6}T\right)\lambda^2}{\lambda^2 - \left(0.0110199 + 0.584758\times10^{-6}T\right)} + \frac{\left(0.91316 + 0.548368\times10^{-6}T\right)\lambda^2}{\lambda^2 - 100}, \tag{8}$$

where T is the temperature (℃) and λ represents the wavelength. The RI of the n_t can be obtained by the following equation [14]

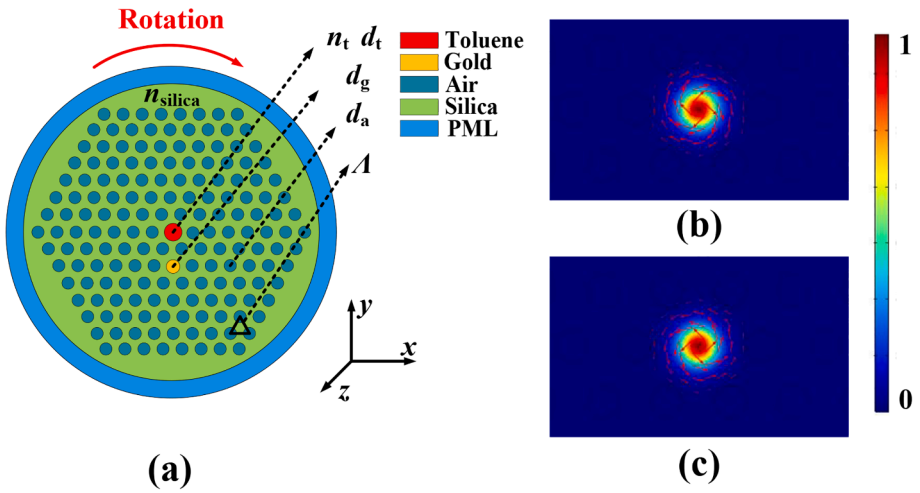

Fig. 2. (a) The two-dimensional diagrammatic sketch of the proposed toluene and gold wire-filled HT-PCF, and (b) and (c) are the Poynting vector distributions of the RCP and LCP of the core mode when the fiber is rotated clockwise.

$$n_t(\lambda) = 1.474775 + \frac{0.00690031}{\lambda^2} + \frac{2.1776 \times 10^{-4}}{\lambda^4} - \sigma(T - 20.15), \quad (9)$$

where $\sigma = 3.94 \times 10^{-4}$ /°C stands for the thermos-optic coefficient of the toluene.

The relative dielectric constant of the gold material (ε_g), which defined by the Drude-Lorentz model can be expressed as [30,31]

$$\varepsilon_g = \varepsilon_\infty - \frac{\omega_D^2}{\omega(\omega - j\gamma_D)} - \frac{\Delta\varepsilon \cdot \Omega_L^2}{(\omega^2 - \Omega_L^2) - j\Gamma_L\omega}, \quad (10)$$

where ε_∞ is the permittivity of the high frequency. ω is the angle frequency of the fiber, and $\Delta\varepsilon$ is the weighted coefficient. Γ_L and Ω_L are the frequency and spectral width of the Lorentz oscillator, respectively. γ_D and ω_D are the damping frequency and plasma frequency, respectively. The values of the detailed parameters in Eq. (9) for ε_g are given in Table.1.

When the phase-matching condition between the core mode and surface plasmon polariton (SPP) mode is satisfied, the sharp confinement loss α_{Loss} peak can be obtained. α_{Loss} peak, which can character the coupling strength between the core mode and the SPP mode, is described as [32]

$$\alpha_{Loss}\ (dB/cm) = 8.686 \times \frac{2\pi}{\lambda} \times Im(n_{eff}) \times 10^4, \quad (11)$$

where Im(n_{eff}) is the imaginary part of the calculated effective RI.

The sensitivity (S) is the important factor to evaluate the sensing performance, and it is defined as [33,34]

$$S\ (nm/^\circ C) = \frac{\Delta\lambda_{peak}}{\Delta T}, \quad (12)$$

The resolution (R) of the sensing is defined as [35]

$$R\ (^\circ C) = \frac{\Delta T \cdot \Delta\lambda_{min}}{\Delta\lambda_{peak}}, \quad (13)$$

where $\Delta\lambda_{peak}$, $\Delta\lambda_{min}$ (0.1 nm), and ΔT denote the resonance wavelength shift, resolution of the detector, and temperature variation, respectively.

Table 1
The parameter values in Eq. (9) for ε_g.

Parameters	ε_∞	$\Delta\varepsilon$	$\omega_D/2\pi$ (THz)	$\Omega_L/2\pi$ (THz)	$\gamma_D/2\pi$ (THz)	$\Gamma_L/2\pi$ (THz)
Values	5.9673	1.09	2113.6	650.07	15.92	104.86

Influence of the structure parameters of the toluene and gold Wire-Filled HT-PCF on the sensing performance

The initial structural parameters of the HT-PCF were set as following: $d_t = 1.9$ μm, $d_g = 0.6$ μm, $d_a = 1.6$ μm, $\Lambda = 3.2$ μm, and $\alpha = 0.004$ rad/μm. Fig. 3(a) and 3(b) show the Poynting vector distributions of the RCP and LCP core modes at 1.65 μm. Fig. 3(c) and 3(d) show the Poynting vector distributions of 1st RCP and 1st LCP SPP modes at 1.65 μm. Fig. 3(e) and 3(f) show the Poynting vector distributions of the RCP and LCP core modes for the resonant condition at 1.689 μm. Fig. 3(g) shows the effective RI curves of the RCP and LCP core modes and 1st LCP and RCP SPP modes, and the α_{Loss} spectra of the LCP and RCP core modes when the initial temperature is set as 20 ℃. From Eqs. (4) and (6), when the fiber is twisted, ε_t and μ_t are not isotropic, so the circular birefringence will appear. As a result, the effective RIs of the RCP and LCP core modes and the 1st order RCP and LCP SPP modes are non-degenerate, respectively. When the twist direction is clockwise, the effective RIs of the RCP core mode and RCP SPP mode are larger than those of the LCP core mode and LCP SPP mode. In addition, the RCP and LCP core modes occur to couple with the 1st order of RCP and LCP SPP modes, respectively. The proposed HT-PCF has a regular hexagonal array, so the resonant wavelength between the RCP core mode and 1st RCP SPP mode, and the LCP core mode and 1st LCP SPP mode are the same. Therefore, for the RCP and LCP core modes, there is little difference for the temperature response. In the following studies, only RCP core mode is investigated.

Fig. 4(a) and 4(b) are the α_{Loss} peak curves of the RCP core modes, when d_t, Λ, and the temperature are changed from 20 to 30 ℃, respectively. From Fig. 4(a), when d_t increases from 1.8 to 2.0 μm at fixed temperature 20 ℃, the α_{Loss} peak wavelength experiences blue shift, which decreases from 1.790 to 1.607 μm. As d_t is increased from 1.8 to 2.0 μm and the temperature is 30 ℃, the α_{Loss} peak wavelength also experiences blue shift, which decreases from 1.950 to 1.753 μm. The α_{Loss} peak values also occur to decrease with the blue shift of the wavelength. It is because that when d_t is increased, the effective RIs of the core modes increase, while the change of effective RIs of the 1st SPP modes is small, so the α_{Loss} peak wavelength will be blue shift. Besides, their effective RI differences become larger, which result in the weaker coupling strength. When d_t increases from 1.8 to 1.9 and 2.0 μm, the temperature sensitivities in the range from 20 to 30 ℃ are 16.0, 15.5, and 14.7 nm/℃ respectively. Thus, the smaller d_t can be chosen to obtain the higher temperature sensitivity. From Fig. 4(b), when Λ increases from 3.0 to 3.4 μm and the temperature is chosen as 20 ℃, the α_{Loss} peak wavelength will be blue-shifted, and the resonant wavelength decrease from 1.697, to 1.686 μm. Their corresponding power of the

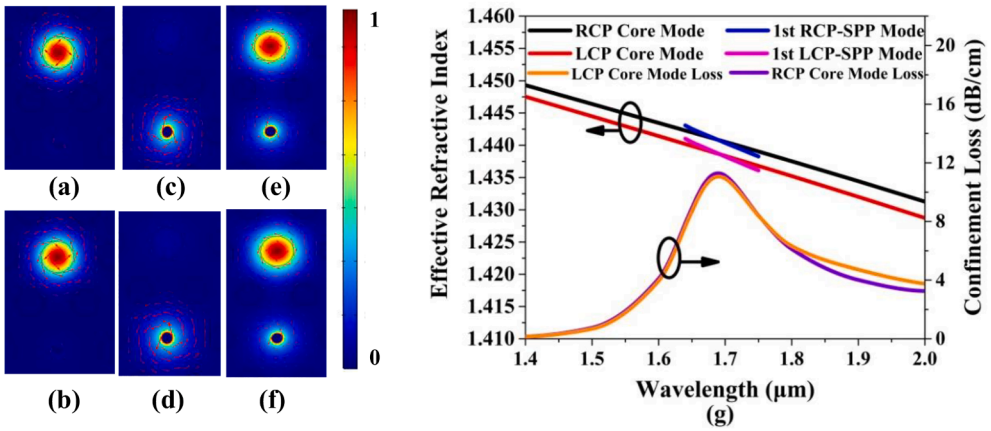

Fig. 3. (a) and (b) The Poynting vector distributions of the RCP and LCP core modes at 1.65 μm. (c) and (d) Poynting vector distributions of 1st RCP and 1st LCP SPP modes at 1.65 μm. (e)-(f) Poynting vector distributions of the RCP and LCP core modes in resonant condition at 1.689 μm. (g) Effective RI curves of the RCP and LCP core modes, 1st LCP and RCP SPP mode and the α_{Loss} spectra of the RCP and LCP core modes when the temperature is set as 20 ℃.

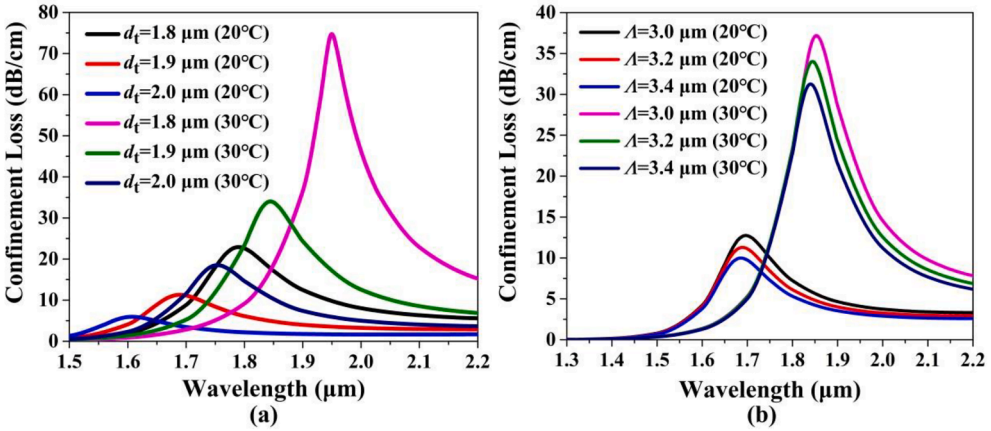

Fig. 4. The α_{Loss} curves of the RCP core mode as (a) d_t is changed from 1.8 to 2.0 μm and (b) Λ is changed from 3.0 to 3.4 μm, when the temperature is chosen as 20 and 30℃, respectively.

α_{Loss} peaks also decrease. When Λ is increased from 3.0 to 3.4 μm and the temperature is set as 30 ℃, the α_{Loss} resonant wavelength also experiences blue shift, and the resonant wavelengths decrease from 1.853 to 1.840 μm, and the α_{Loss} peak values decrease. The direct cause is that when Λ is increased, the calculated effective RIs of the RCP core mode and the corresponding RCP SPP mode increase, and the RI change of the RCP core mode is larger, so the α_{Loss} peak wavelength experiences blue shift. Besides, the distance between the core region and gold wire increases, so the coupling strength becomes weaker. When Λ increases from 3.0 to 3.4 μm, the temperature sensitivities in the range from 20 to 30 ℃ can reach 15.6, 15.5, and 15.4 nm/℃. Thus, the change of Λ has limited effect on the temperature sensitivity, and the smaller Λ can be

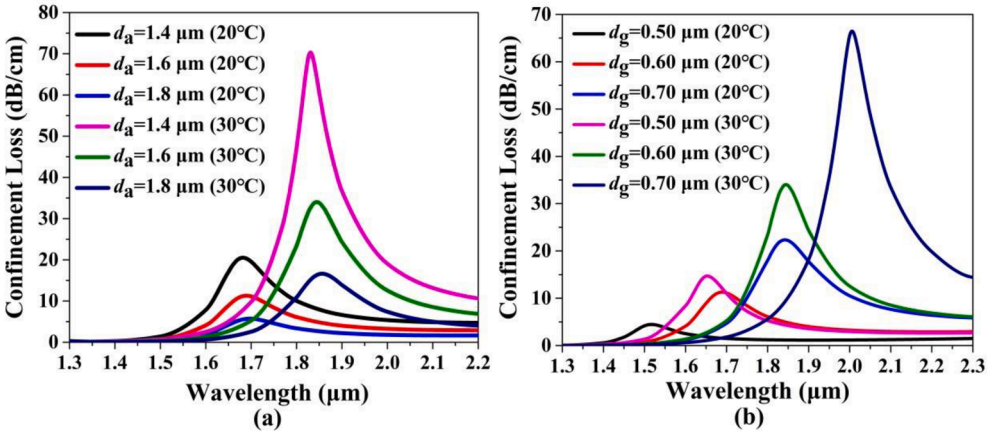

Fig. 5. The α_{Loss} curves of the RCP core mode as (a) d_a is changed from 1.4 to 1.8 μm and (b) d_g is changed from 0.50 to 0.70 μm, when the temperature is chosen as 20 and 30℃, respectively.

chosen to obtain the higher temperature sensitivity.

Fig. 5(a) and 5(b) are the α_{Loss} peak curves of the RCP core modes, when d_a and d_g are changed to different values, respectively. As seen from Fig. 5(a), when d_a increases from 1.4 to 1.8 μm at fixed temperature 20 ℃, the α_{Loss} peak wavelength experiences red shift, which increases from 1.682 to 1.697 μm. The α_{Loss} peak value experiences a decrease trend. When d_a increases from 1.4 to 1.8 μm at fixed temperature 30 ℃, the α_{Loss} peak wavelength experiences red shift, which increases from 1.831 to 1.856 μm. The α_{Loss} peak value also experiences a decrease. It is because that when d_a is increased, the effective RIs of the RCP core mode and corresponding SPP mode decrease. It is because that the compared with the SPP mode, the effective RI reduction degree of the RCP core mode is larger, the α_{Loss} peak wavelength experiences red shift. In addition, the effective RI difference between the two modes gradually becomes large. When d_a increases from 1.4 to 1.8 μm, the temperature sensitivity in the range from 20 to 30 ℃ increase from 14.9 to 15.9 nm/℃. Thus, the larger d_a can be chosen to obtain the higher temperature sensitivity. As seen in Fig. 5(b), when d_g increases from 0.5 to 0.7 μm at fixed temperature 20 ℃, the α_{Loss} peak wavelength experiences red shift, which increases from 1.571 to 1.842 μm. The α_{Loss} peak value experiences an increase. When d_g increases from 0.5 to 0.7 μm at fixed temperature 30 ℃, the α_{Loss} peak wavelength experiences red shift, which increases from 1.653 to 2.006 μm. The α_{Loss} peak value also experiences an increase. It is because that when d_g increases, the effective RIs of the SPP mode increases while the effective RIs of the RCP core mode remain unchanged, so the α_{Loss} peak wavelength experiences red shift. Besides, as d_g increases, their effective RI difference gets smaller. When d_g increases from 0.5 to 0.7 μm, the temperature sensitivity in the range from 20 to 30 ℃ can increase from 13.6 to 16.4 nm/℃. Thus, the larger d_g can be chosen to obtain the higher temperature sensitivity.

Fig. 6 shows the α_{Loss} peak curves of the RCP core modes, when α and temperature are changed, respectively. From Fig. 6, when α increases from 0.002 to 0.006 rad/μm at fixed temperature 20 ℃, the α_{Loss} peak wavelength experiences red shift, which increases from 1.670 to 1.724 μm. The α_{Loss} peak value experiences an increase. When α increases from 0.002 to 0.006 rad/μm at fixed temperature 30 ℃, the α_{Loss} peak wavelength experiences red shift, which increases from 1.821 to 1.886 μm. The α_{Loss} peak value also experiences an increase. It is because that when α is increased, their effective RIs of the RCP core mode and corresponding SPP mode increase. Moreover, compared with the SPP mode, the effective RI increment is less, the α_{Loss} peak wavelength experiences red shift. When d_a increases from 0.002 to 0.006 rad/μm, the temperature sensitivities in the range from 20 to 30 ℃ can reach 15.1, 15.5, and 16.2 nm/℃, respectively. Comparing with the traditional PCFs, α is an additional parameter. It is proved that the larger d_a is conducive to obtain the higher temperature sensitivity.

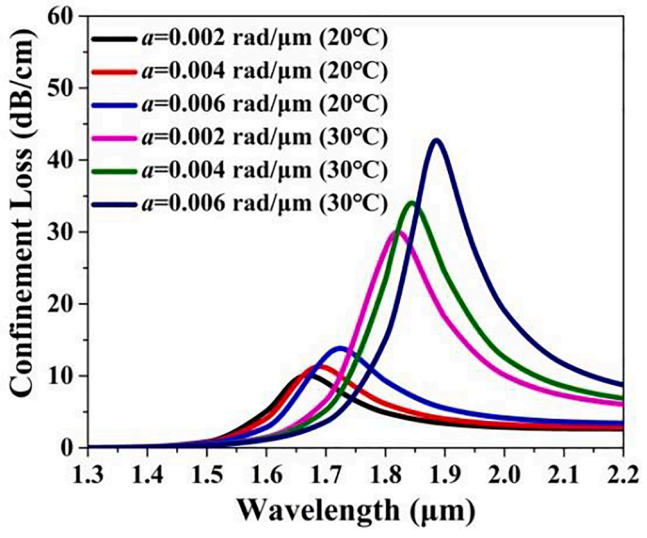

Fig. 6. The α_{Loss} curves of the RCP core mode, as α is changed from 0.002 to 0.006 rad/μm, when the temperature is chosen as 20 and 30℃, respectively.

Temperature sensing performance of the toluene and gold wire filled HT-PCF

By the above analysis, the optimized structure parameters of the proposed toluene and gold wire-filled HT-PCF are chosen as following: $d_t = 1.8$ μm, $\Lambda = 3.0$ μm, $d_a = 1.8$ μm, $d_g = 0.7$ μm, and $\alpha = 0.005$ rad/μm. In the following, the temperature sensing sensitivity, resolution, and linearity of the toluene and gold wire-filled HT-PCF in the range of −20 to 20 ℃ and 20 to 70 ℃ will be investigated, respectively. Fig. 7(a) shows the α_{Loss} curves of the RCP core mode, when the temperature changes from −20 to 20 ℃. It can be seen from Fig. 7(a) that as the temperature increases, the α_{Loss} peak wavelength experiences red shift and the α_{Loss} peak value increases. It is because that the RI of the toluene and the effective RI of the RCP core mode decrease as the temperature increases while the RCP 1st SPP mode changes little. Thus, the effective RI differences between the RCP core mode and RCP 1st SPP mode will reduce, and the coupling strength becomes stronger. Fig. 7(b) shows the corresponding fitting results between the α_{Loss} peak wavelength and temperature. In Fig. 7(b), we can see that the resonant wavelengths in the temperature range of −20 to 20 ℃ are located at 1.423, 1.537, 1.673, 1.828, and 1.995 μm, respectively. The corresponding temperature sensitivities are 11.4, 13.6, 15.5, and 16.7 nm/℃, respectively. In addition, the linear fitting result is $y = 0.01435x + 1.6912$, so we can obtain that the average sensitivity of the proposed HT-PCF is 14.35 nm/℃, and the linearity is 0.993.

Fig. 8(a) shows the α_{Loss} curves of the RCP core mode, when the temperature changes from 20 to 70 ℃. It can be seen in Fig. 8(a) that when the is temperature increased, the α_{Loss} peak wavelength experiences red shifts and the corresponding α_{Loss} peak value was increased in the temperature range of 20 to 40 ℃ and then decrease in the temperature range of 40 to 70 ℃. It is because that as the wavelength increases, the effective RI difference between the RCP core mode and 1st SPP mode decreases gradually in the temperature range of 20 to 40 ℃. In contrast, in the temperature range of 40 to 70 ℃, their effective RI difference increases with the increase of wavelength. Fig. 8(b) shows the corresponding fitting results between the α_{Loss} peak wavelength and temperature. As seen from Fig. 8(b), the resonant wavelengths in the temperature range of 20 to 70 ℃ are located at 1.995, 2.164, 2.339, 2.519, 2.691, and 2.853 μm, respectively. The corresponding temperature sensitivities are 16.9, 17.5, 18.0, 17.2, and 16.2 nm/℃, respectively. In addition, the linear fitting result is $y = 0.01729x + 1.64885$, so the average sensitivity can be up to 17.29 nm/℃, and $R^2 = 0.999$, which shows the good linearity for the temperature sensitivity.

Fig. 9(a) is the changes of the sensitivity and resolution in the temperature ranges of −20 to 20 ℃. From Fig. 9(a), with the increase of the temperature, the sensitivity increases monotonously, and the resolution decreases monotonously. The lowest and highest sensitivities are 11.4 and 16.7 nm/℃ in the range of −20 to −10 ℃ and 10 to 20 ℃, respectively. So their corresponding resolutions are 5.99×10^{-3} and 8.77×10^{-3} ℃, respectively. Fig. 9(b) shows the changes of the sensitivity and resolution in 20 to 70 ℃. From Fig. 9(b), when the temperature increases, the sensitivity first increases and then decreases, and the variation trend of the resolution is also opposite to that of the sensitivity. The lowest and highest sensitivities are 16.2 and 18.0 nm/℃ in the temperature range of 60 to 70 ℃ and 40 to 50 ℃, respectively. The corresponding resolutions values are 5.56×10^{-3} and 6.17×10^{-3} ℃ in the temperature range of 40 to 50 ℃ and 60 to 70 ℃, respectively.

Hydrostatic pressure influence of the toluene and gold Wire-Filled HT-PCF

Hydrostatic pressure, which is considered as an omni-directional

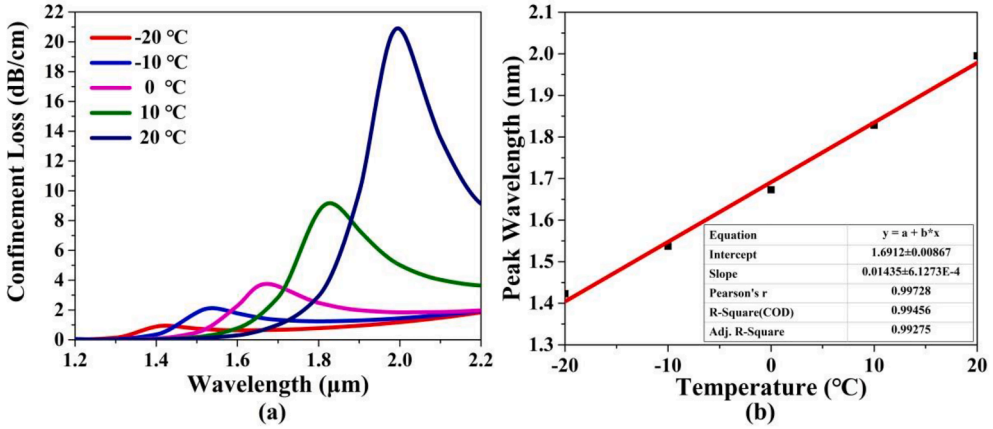

Fig. 7. (a) The α_{Loss} curves of the RCP core mode, when the temperature changes from −20 to 20℃, and (b) the corresponding fitting results between the α_{Loss} peak wavelength and temperature.

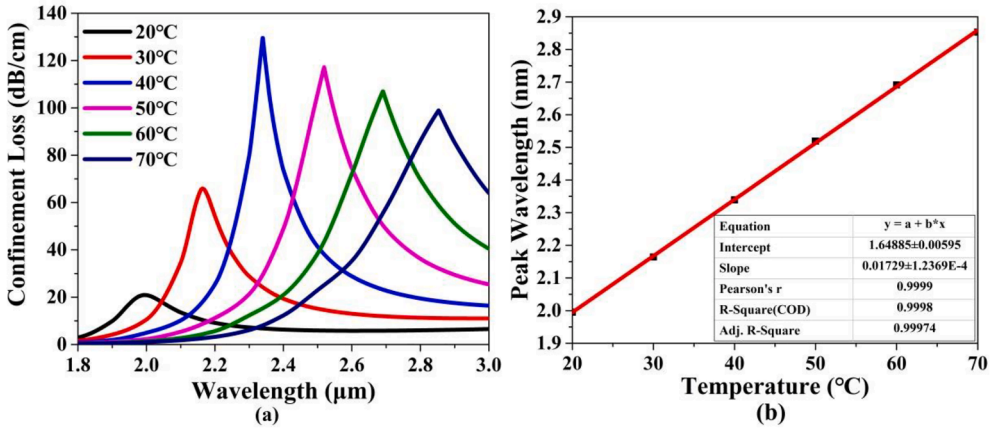

Fig. 8. (a) The α_{Loss} curves of the RCP core mode of the toluene and gold wire-filled HT-PCF when the temperature changes from 20 to 70℃, and (b) the corresponding fitting results between the α_{Loss} peak wavelength and temperature.

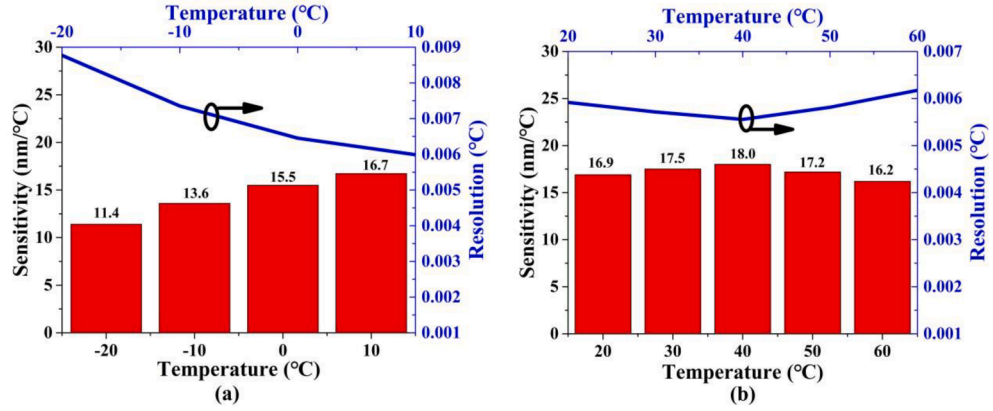

Fig. 9. The changes of the sensitivity and resolution in the temperature range of (a) −20 to 20 ℃ and (b) 20 to 70 ℃, respectively.

force, widely exists in the deep crust, dams, and oceans. Thus, as a temperature sensor, the hydrostatic pressure's cross-sensitivity influence should be considered. According to the photoelastic effect, the hydrostatic pressure-dependent n_{silica} can be described as [36]

$$\begin{aligned} n_x &= n_{\text{silica}} - K_1\sigma_x - K_2(\sigma_y + \sigma_z) \\ n_y &= n_{\text{silica}} - K_1\sigma_y - K_2(\sigma_x + \sigma_z) \\ n_z &= n_{\text{silica}} - K_1\sigma_z - K_2(\sigma_x + \sigma_y) \end{aligned} \tag{13}$$

where σ_x, σ_y, and σ_z stand for the pressure components in the x, y and z direction. In this simulation, $E_{silica} = 73.1$ GPa (Yong's modulus), and $\upsilon = 0.17$ (Poisson's ratio) of the silica are used. Thus, $K_1 = 6.5 \times 10^{-13}$ m^2/N, and $K_2 = 4.2 \times 10^{-12}$ m^2/N [37,38].

Fig. 10(a) and 10(b) show the α_{Loss} curves and the corresponding fitting results between the α_{Loss} peak wavelength and hydrostatic pressure when the hydrostatic pressure changes from 0 to 50 Mpa and the temperature is chosen as 20 ℃. From Fig. 10(a), when the hydrostatic

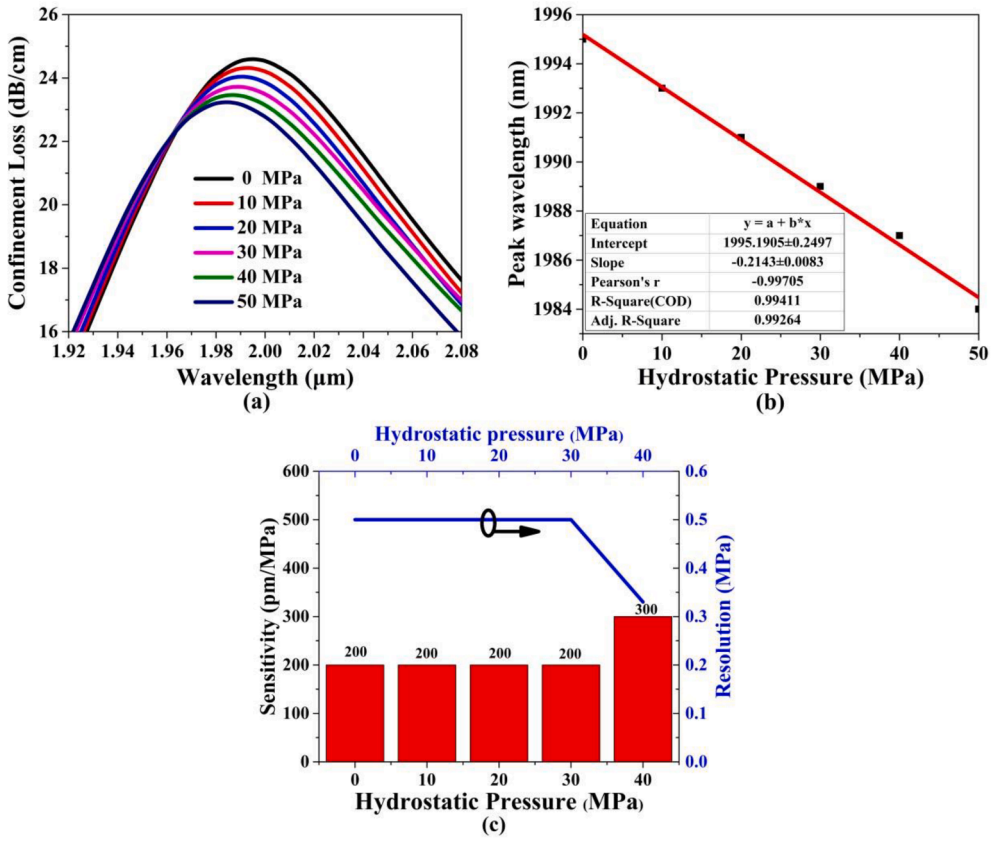

Fig. 10. (a) The α_{Loss} curves of the RCP core mode of the toluene and gold wire-filled HT-PCF when the hydrostatic pressure changes from 0 to 50 MPa. (b) The corresponding fitting results between the α_{Loss} peak wavelength and hydrostatic pressure. (c) The changes of the sensitivity and resolution with the hydrostatic pressure.

pressure is increased, the α_{Loss} peak wavelength experiences blue shift, and the α_{Loss} peak value experiences a decrease. When the hydrostatic pressure increases from 0 to 50 MPa, the corresponding peak wavelengths are 1995, 1993, 1991, 1989, 1987, and 1984 nm, respectively. The main reason can be considered that when the hydrostatic pressure is increased, the RCP core mode and corresponding 1st RCP SPP mode's effective RIs decrease, and the effective RI reduction degree of the SPP mode is larger. Meanwhile, due to the effective RI reduction degree of the SPP mode is larger than that of the RCP core mode and their effective RI difference becomes larger, so the α_{Loss} peak value decreases gradually. From Fig. 10(b), the average hydrostatic pressure sensitivity is −214.3 pm/MPa, and the value of R^2 can achieve 0.994. The sensitivity of the temperature sensing is two orders of magnitude higher than that of the hydrostatic pressure, which means that the cross-sensitivity has little effect. Fig. 10(c) shows the change trends of the hydrostatic pressure sensitivities and corresponding resolutions in the hydrostatic pressure ranges of 0 to 50 MPa. The sensitivity is maintained at 200 pm/MPa in the range of 0 to 40 MPa and then increases to 300 pm/MPa in the range of 40 to 50 MPa. The resolution is also maintained at 0.5 MPa in the range of 0 to 40 MPa and then decreases to 0.33 MPa in the range of 40 to 50 MPa. The comparisons between the designed toluene and gold wire-filled HT-PCF with other previous works are shown in Table 2. As seen from Table 2, the proposed HT-PCF shows better performances for the temperature sensing.

Fabrication processes of the toluene and gold Wire-Filled HT-PCF temperature sensor

The schematic diagram of the fabrication process of the proposed toluene and gold wire-filled HT-PCF is shown in Fig. 11. The fabrication process can be divided into the two parts: 1) fabricate the gold wire-filled HT-PCF by the stack and draw technique [39-41]; 2) selectively fill the toluene into the central air hole by the multi-step filling technique [14,21,42].

Table 2
Comparison results between the proposed toluene and gold wire-filled HT-PCF with other works

Refs	Fiber Structures	Temperature ranges (℃)	|Sensitivities| (nm/℃)	Resolutions(℃)
[11]	TSL filled and gold-coated PCF	20–80	2.15	N/A
[12]	Water-filled dual core PCF	25–50	1.23	N/A
[13]	Toluene-filled bandgap-like PCF	25–31	1.747	N/A
[14]	Toluene-filled PCF	0–90	6.25	3.32×10^{-3}
[15]	Toluene-filled and gold-coated PCF	20–100	6.51	N/A
[16]	TSL-filled and gold-coated PCF	20–30	6.83	2.9×10^{-3}
[17]	Gold-coated D-shaped PCF	0–60	10.61	N/A
[18]	Glycerin-filled PCF	−25–85	1.5005	1.33×10^{-2}
This work	Toluene and gold wire-filled HT-PCF	−20–20	14.35	8.87×10^{-3}6.17 $\times 10^{-3}$
		20–70	17.29	

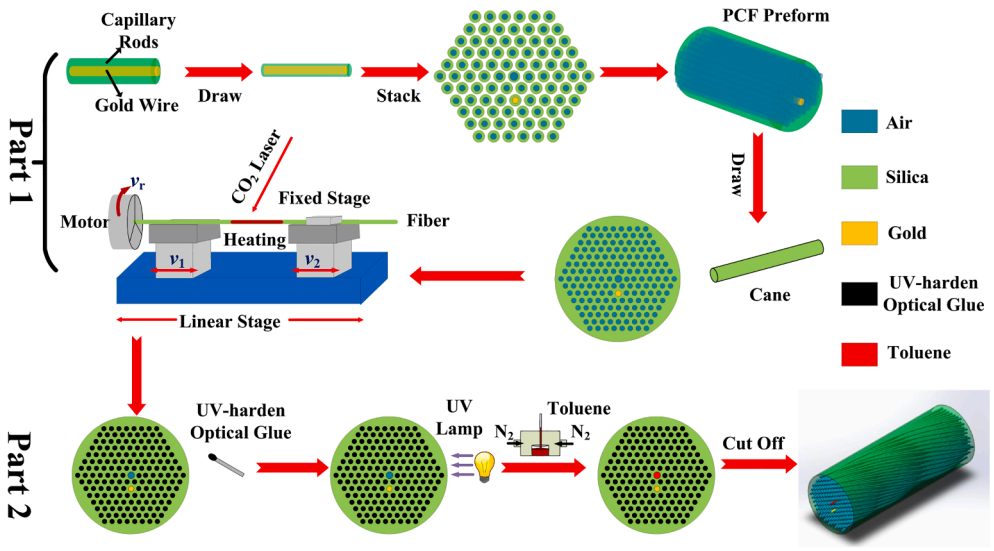

Fig. 11. The fabrication processes of the proposed toluene and gold wire-filled HT-PCF.

For the first part, a metallic wire will be used to push the gold wire into the silica capillary. Second, the gold wire-filled silica capillary is drawn to form a thin gold filled capillary. In this way, the silica can wrap the gold wire. Third, the silica capillaries and gold capillary are stacked to form the desired structure. In this process, we can use a hexagonal mold to stack each hollow capillary silica tube into the designed structure. It should be noted that the gap between capillaries can be filled with solid silica rods. Fourth, the whole arranged structure is put into a larger silica tube to form the PCF preform. In the previous step, we stack the capillary quartz tubes into a regular hexagon, while the larger silica tube is cylindrical, so we also need to fill many solid silica rods in the gap. Fifth, the gold wire-filled PCF cane can be obtained by drawing the preform. Under CO_2 laser heating, through post-processing, permanent distortion can be applied to the undistorted PCF. Sixth, place a length of the PCF between a motorized rotating table and a fixed table. The speeds of the rotation motor is set as v_r, and the movement speeds of the left and right electric displacement platforms are set as v_1 and v_2, respectively. In order to keep the fiber straight during the whole processing, the translation speeds of v_1 and v_2 are set to be equal. Seventh, use a CO_2 laser to heat the PCF. As the motor rotates, the focused laser beam can scan along the PCF. By using a shutter and galvanometer-based variable attenuator, the laser power and the exposure time can be adjusted. Through the cooperation of CO_2 laser system and electric displacement platform, the target twist period and sample length can be achieved [43]. In recent years, some helical twist fibers have been fabricated [44-46]. In our design, the value of d_g/Λ is designed to be only 0.233 in order to reduce the difficulty of the drawing and twist process.

The second part is to fill the toluene into the central air hole. First, a metal tip is used to dip a small amount of UV curable glue, and then adjust the relative position of the PCF end face and the metal tip to seal the cladding air holes. There are many choices of UV curable glue. Here, we choose the UV curable glue with good fluidity (15 cps can be found in Norland), which can help to seal every air hole. Second, a UV lamp is used to cure the UV curable glue at the end face of the fiber. Third, put one end of the fiber into the toluene liquid, and then use a pump to pump the toluene into the central air hole. Finally, cut off the sealed part of the fiber to obtain the proposed toluene and gold wire-filled HT-PCF.

Conclusions

In conclusion, a toluene and gold wire-filled HT-PCF temperature sensor is proposed and theoretically investigated. After optimizing the HT-PCF's structure parameters, the average sensitivities can reach 14.35 and 17.29 nm/℃ in the temperature range from −20 to 20 ℃, 20 to 70 ℃, respectively. The corresponding highest temperature resolutions are 8.87×10^{-3} and 6.17×10^{-3} ℃, respectively. The proposed temperature is hydrostatic pressure incentive with an average sensitivity of only −214.3 pm/MPa in the hydrostatic pressure range of 0 to 50 MPa. The fabrication process of the toluene and gold wire-filled HT-PCF temperature sensor is proposed. It is believed that the proposed temperature sensor has potential applications in many fields such as environmental monitoring, etc.

CRediT authorship contribution statement

Shi Qiu: Conceptualization, Formal analysis, Writing – original draft, Methodology, Investigation. **Jinhui Yuan:** Supervision, Formal analysis, Methodology, Writing - review & editing. **Sainan Duan:** Supervision, Formal analysis, Writing - review & editing. **Xian Zhou:** Supervision, Formal analysis, Writing - review & editing. **Chao Mei:** Formal analysis, Writing - review & editing. **Yuwei Qu:** Formal analysis. **Binbin Yan:** Formal analysis, Writing - review & editing. **Qiang Wu:** Supervision, Formal analysis, Methodology, Writing - review & editing. **Kuiru Wang:** Formal analysis. **Xinzhu Sang:** Supervision, Writing - review & editing. **Keping Long:** Supervision, Writing - review & editing. **Chongxiu Yu:** Supervision, Writing - review & editing.

Declaration of Competing Interest

The authors declare that they have no known competing financial interests or personal relationships that could have appeared to influence the work reported in this paper.

Acknowledgments

This work is supported by National Natural Science Foundation of China (Granted No. 61935007).

References

[1] Birks TA, Knight JC, St P, Russell J. Endlessly single-mode photonic crystal fiber. Opt. Lett 1997;22(13):961–3.
[2] Hameed MFO, Azab MY, Heikal AM, et al. Highly Sensitive Plasmonic Photonic Crystal Temperature Sensor Filled With Liquid Crystal. IEEE Photon. Technol. Lett 2016;28(1):59–62.
[3] G.K.L Wong. Excitation of Orbital Angular Momentum Resonances in Helically Twisted Photonic Crystal Fiber. Science 2012;337(6093):446–9.

[4] Shin W, Lee Y, Yu BA, et al. Spectral characterization of helicoidal long-period fiber gratings in photonic crystal fibers. Opt. Commun 2009;282(17):3456–9.
[5] Zhang F, Wang Y, Bai Z, et al. Helicity Enhanced Torsion Sensor Based on Liquid Filled Twisted Photonic Crystal Fibers. Sensors 2020;20(5):1490.
[6] Xi X, Gordon KLW, Thomas W, St P, Russell J. Measuring mechanical strain and twist using helical photonic crystal fiber. Opt. Lett 2013;38(24):5401–4.
[7] Dong X, Chu BCB. Phase drift compensation for electric current sensor employing a twisted fiber or a spun highly birefringent fiber. IEEE J Sel Top Quantum Electron 2000;6(5):803–9.
[8] Beravat R, Wong GK, et al. Current sensing using circularly birefringent twisted solid-core photonic crystal fiber. Opt. Lett 2016;41(7):1672–5.
[9] Weng S, Pei L, Wang J, et al. High sensitivity D-shaped hole fiber temperature sensor based on surface plasmon resonance with liquid filling. Photon. Res 2017;5 (2):103–7.
[10] Lu M, Zhang X, Liang Y, et al. Liquid crystal filled surface plasmon resonance thermometer. Opt. Express 2016;24(10):10904.
[11] Liu Q, Li S, Chen H, et al. High-sensitivity plasmonic temperature sensor based on photonic crystal fiber coated with nanoscale gold film. Appl. Phys. Express 2015;8 (4):046701.
[12] Liu S, Wang Z, Hou M, et al. Asymmetrically infiltrated twin core photonic crystal fiber for dual-parameter sensing. Opt. Laser Technol 2016;82:53–6.
[13] Yang X, Lu Y, Liu B, et al. Fiber Ring Laser Temperature Sensor Based on Liquid-Filled Photonic Crystal Fiber. IEEE Sens. J 2017;17(21):6948–52.
[14] Ma J, Yu H, Jiang X, et al. High-performance temperature sensing using a selectively filled solid-core photonic crystal fiber with a central air-bore. Opt. Express 2017;25(8):9406–15.
[15] Yang X, Lu Y, Liu B, et al. High Sensitivity Hollow Fiber Temperature Sensor Based on Surface Plasmon Resonance and Liquid Filling. IEEE Photon. J 2018;10(2):1–9.
[16] Han B, Zhang Y. Siyu E, et al, Simultaneous measurement of temperature and strain based on dual SPR effect in PCF. Opt. Laser Technol 2019;113:46–51.
[17] Liu Y, Jing X, Li S, et al. High-sensitivity plasmonic temperature sensor based on gold-coated D-shaped photonic crystal fiber. Appl. Opt 2019;58(18):5115.
[18] Zhao J, Zhao Y, Bai L, et al. Sagnac Interferometer Temperature Sensor Based on Microstructured Optical Fiber Filled with Glycerin. Sens. Actuat. Phys 2020;314: 112245.
[19] Li J, Fan P, Sun L, et al. Few-period helically twisted all-solid photonic bandgap fibers. Opt. Lett 2018;43(4):655–8.
[20] Jiang X, Lu P, Sun Y, et al. Simultaneous measurement of axial strain and temperature based on twisted fiber structure. Chin Opt Lett 2018;16(4):040602.
[21] Khanikar T, De M, Singh VK. A review on infiltrated or liquid core fiber optic SPR sensors. Photonic Nanostruct 2021;46(296):100945.
[22] Nicolet A, Zolla F, Agha YO, et al. Leaky modes in twisted microstructured optical fibers. Waves Random Complex Media 2007;17(4):559–70.
[23] Li B, Zhou G, Liu J, Xia C, Hou Z. Orbital-angular-momentum-amplifying helical vector modes in $Yb3^{+}$-doped three-core twisted microstructure fiber. Opt. Express 2020;28(14):21110–20.
[24] Nakano S, Fujisawa T, Saitoh K. The Effect of Core Offset on the Mode Converting Characteristics in Twisted Single Mode Fibers. J. Lightwave Technol 2019;37(21): 5479–85.
[25] Takeshi Fujisawa. Kunimasa, Off-axis core transmission characteristics of helically twisted photonic crystal fibers. Opt. Lett 2018;43(20):4935–8.
[26] Chen L, Zhang W, et al. Photonic crystal fiber polarization rotator based on the topological Zeeman effect. Opt. Lett 2015;40(15):3448–51.
[27] Ye J, Li Y, Han Y, Deng D, Guo Z, Gao J, et al. Excitation and separation of vortex modes in twisted air-core fiber. Opt. Express 2016;24(8):8310–6.
[28] Ghosh G, Endo M, Iwasaki T. Temperature-dependent sellmeier coefficients and chromatic dispersions for some optical fiber glasses. J. Lightwave Technol 1994;12 (8):1338–42.
[29] Qiu S, Yuan J, Zhou X, et al. Highly sensitive temperature sensing based on all-solid cladding dual-core photonic crystal fiber filled with the toluene and ethanol. Opt. Commun 2020;477:126357.
[30] Liu Y, Li S, Chen H, Li J, Zhang W, Wang M. Surface Plasmon Resonance Induced High Sensitivity Temperature and Refractive Index Sensor Based on Evanescent Field Enhanced Photonic Crystal Fiber. J. Lightwave Technol 2020;38(4):919–28.
[31] Qu Y, Yuan J, Zhou X, et al. A V-shape photonic crystal fiber polarization filter based on surface plasmon resonance effect. Opt. Commun 2020;452:1–6.
[32] Jiang L, Zheng Y, Hou L. Zheng K, Peng J, Zhao X, An ultrabraoadband polarization splitter based on square-lattice dual-core photonic crystal fiber with a gold wire. Opt. Commun 2015;351:50–6.
[33] Luan N, Ding C, Yao J. A Refractive Index and Temperature Sensor Based on Surface Plasmon Resonance in an Exposed-Core Microstructured Optical Fiber. IEEE Photon. J 2016;8(2):1–8.
[34] Siddik AB, Hossain S, Paul AK, et al. High sensitivity property of dual-core photonic crystal fiber temperature sensor based on surface plasmon resonance. Sens Bio-Sens Res 2020;29:100350.
[35] Liang H, Shen T, Feng Y, Xia Z, Liu H. A Surface Plasmon Resonance Temperature Sensing Unit Based on a Graphene Oxide Composite Photonic Crystal Fiber. IEEE Photon. J 2020;12(3):1–11.
[36] Chen D, Hu G, Chen L. Dual-Core Photonic Crystal Fiber for Hydrostatic Pressure Sensing. IEEE Photon. Technol. Lett 2011;23(24):1851–3.
[37] Szpulak M, Martynkien T, Urbanczyk W. Effects of hydrostatic pressure on phase and group modal birefringence in microstructured holey fibers. Appl. Opt 2004;43 (24):4739–44.
[38] Liu Z, Tse MLV, Wu C, Chen D, Lu C, Tam HY. Intermodal coupling of supermodes in a twincore photonic crystal fiber and its application as a pressure sensor. Opt. Express 2012;20(19):21749–57.
[39] Pniewski J, Kasztelanic R, Nowosielski JM, Filipkowski A, Piechal B, Waddie AJ, et al. Diffractive optics development using a modified stack-and-draw technique. Appl. Opt 2016;55(18):4939–45.
[40] Lee HW, Schmidt MA, Russell RF, Joly NY, Tyagi HK, Uebel P, et al. St.J Russell, Pressure-assisted melt-filling and optical characterization of Au nano-wires in microstructured fibers. Opt. Express 2011;19(13):12180–9.
[41] H. Lee Plasmonic photonic crystal fiber, Ph.D. dissertation, Max Plank Inst. Sci 2012 Light, Erlangen, Germany.
[42] Hoang VT, Kasztelanic R, Anuszkiewicz A, Stepniewski G, Filipkowski A, Ertman S, et al. All-normal dispersion supercontinuum generation in photonic crystal fibers with large hollow cores infiltrated with toluene. Opt. Mater. Express 2018;8: 3568–82.
[43] Chen W, Chen Z, Qiu Y, Kong L, Lin H, Jia C, et al. Highly sensitive optical fiber curvature sensor based on a seven-core fiber with a twisted structure. Appl. Opt 2019;58(32):8776–84.
[44] Jiang X, Lu P, Hao L, Ni W, Zhang J. Simultaneous measurement of axial strain and temperature based on twisted fiber structure. Chin. Opt. Lett 2018;16(4):040602.
[45] Xi X, Wong GKL, Frosz MH, Babic F, Ahmed G, Jiang X, et al. Russell, Orbital-angular-momentum-preserving helical Bloch modes in twisted photonic crystal fiber. Optica 2014;1(3):165–9.
[46] Roth P, Chen Y, Günendi MC, Beravat R, Edavalath NN, Frosz MH, et al. Strong circular dichroism for the HE_{11} mode in twisted single-ring hollow-core photonic crystal fiber. Optica 2018;5(10):1315–21.